NIH Public Access
Author Manuscript
J Opt Soc Am A Opt Image Sci Vis. Author manuscript; available in PMC 2013 April 03.

Published in final edited form as:
J Opt Soc Am A Opt Image Sci Vis. 2013 January 1; 30(1): 51–59.

Robust spectral-domain optical coherence tomography speckle model and its cross-correlation coefficient analysis

Xuan Liu[1,*], **Jessica C. Ramella-Roman**[2], **Yong Huang**[1], **Yuan Guo**[1,3], and **Jin U. Kang**[1]

[1]Department of Electrical and Computer Engineering, The Johns Hopkins University, Baltimore, MD, 21218 USA

[2]Department of Biomedical Engineering, The Catholic University of America, Washington, DC, 20064 USA

[3]College of Computer and Control Engineering, Qi Qihar University, Hei Longjiang, 161006 China

Abstract

In this study, we proposed a generic speckle simulation for optical coherence tomography (OCT) signal, by convolving the point spread function (PSF) of the OCT system with the numerically synthesized random sample field. We validated our model and used the simulation method to study the statistical properties of cross-correlation coefficients (XCC) between Ascans which have been recently applied in transverse motion analysis by our group. The results of simulation show that over sampling is essential for accurate motion tracking; exponential decay of OCT signal leads to an under estimate of motion which can be corrected; lateral heterogeneity of sample leads to an over estimate of motion for a few pixels corresponding to the structural boundary.

1. Introduction

Illuminating an object with a coherent light source leads to images with a speckle pattern [1,2]. Optical coherence tomography (OCT) uses light sources with high spatial coherence; therefore, speckle exists ubiquitously in OCT images, as it is in other coherent imaging modalities [3].

In OCT, speckle reduces image contrast; therefore it makes fine anatomic structures indiscernible and tissue boundaries blurred. As a result, speckle is often considered as noise that degrades image quality. Over the years, researchers have developed various methods to suppress speckle noise in OCT images [4–10], which include hardware compounding and digital signal processing approaches. However, speckle also carries information and can be considered as signal. For example, studies have shown tissue type differentiation is possible by analyzing speckle texture in OCT images [11–13]. OCT speckle can also be used to infer tissue or probe dynamics. For example, temporal speckle variance of OCT signal was used to detect blood flow [14–19]. In addition, speckle decorrelation was used to correct scanning speed in manually scanned OCT [20, 21].

Whether or not speckle is being considered as noise or signal, it is a random phenomenon; therefore, a comprehensive study of speckle statistics in OCT could be beneficial for both the suppression of speckle noise as well as the extraction of information from speckle. The statistical properties of OCT speckle have been investigated previously [3, 4, 22, 23]. In those studies, OCT signal at different pixels are considered as statistically independent random variables. However, none of the previous studies considered the point spread

*Corresponding author: xliu35@jhu.edu.

NIH-PA Author Manuscript
NIH-PA Author Manuscript
NIH-PA Author Manuscript

NIH-PA Author Manuscript

NIH-PA Author Manuscript

NIH-PA Author Manuscript

function (PSF) of an OCT system, which plays a critical role in the formation of OCT images. Due to the finite dimension of PSF, OCT signals at neighboring pixels are correlated rather than independent [19, 20]. In our previous work, we utilized such correlation to estimate lateral displacement and demonstrated great potential of this technique toward the development of simple, miniature and light-weight hand-held OCT probes [20].

As suggested by early laser speckle studies, it is difficult to theoretical derive a closed-form probability density function for a speckle pattern convolved with a PSF [1]. Alternatively, numerical simulation can be performed to study speckle statistics with known properties of the imaging system used. For example, a model involving system PSF was established to simulate speckle patterns in ultrasound for motion analysis [24]. Band-limited speckle patterns were also numerically synthesized and used to study the properties of OCT signal [25, 26]. In this manuscript, we proposed a generic simulation method which incorporates the PSF of OCT system to study speckle in OCT. The method is based on Fourier domain OCT (FD OCT) since it is the most popular form of OCT due to its superior sensitivity and imaging speed. However, results obtained based on a FD OCT schematic can still be applied to time domain OCT (TD OCT) with minimal modifications. Using the method, one can generate speckle patterns from any arbitrary system PSF and sample structure. This provides a convenient means to study speckle properties in different imaging conditions. Particularly, our study focused on the statistics of cross correlation coefficient (XCC) between Ascans. XCC were used to estimate lateral displacement in our previous work and a more comprehensive appreciation of the statistical properties of XCC would help evaluating the stability and accuracy of our speckle decorrelation algorithm [20].

This manuscript is organized as follows: first we develop a theoretical model for speckle analogous to the model established for ultrasound imaging systems [23]; afterwards, we verify the model by comparing the probability density function (PDF) and power spectral density (PSD) of speckled image obtained from our simulation with results obtained from a different speckle simulation method proposed by D. Duncan *et al* [25, 26]; finally we use our simulation to study the statistics of XCC in various imaging conditions.

2. Theory

A speckled OCT signal can be synthesized by convolving sample field reflectivity with the PSF of OCT system's, similar to J. Meunier *et al*'s simulation method in ultrasound image [23]. In this manuscript, we use a Cartesian coordinate system (x, y, z) to describe the 3D space. z indicates the axial direction; x is the lateral direction of Bscan. We assume the scanning of OCT sample beam is limited in x-z plane. As a result, the coordinate y stays constant for a Bscan and we can arbitrarily choose the origin of the coordinate system so that y=0 for the Bscan of interest.

In a FD OCT system, the interference signal is detected in the spectral domain. The interference term of the spectrum is denoted as $S(x,k)$ and k is wavenumber ($k=2\pi/\lambda$, λ is wavelength). The coordinate y is omitted because we assume that y=0 which implies a B-mode imaging. Denote the sample field reflectivity at location (x,y,z) as $r_s(x,y,z)$, which can be considered as the three dimensional (3D) object. For OCT system, axial reflectance profile $r_a(z)$ can be considered as the convolution of $r_s(x,y,z)$ with $h_{x,y}(x,y)$. This is because the axial PSF of OCT $h_z(z)$ and the lateral PSF $h_{x,y}(x,y)$ in general are separable. Axial and lateral PSFs are governed by different physical principles: the axial PSF is determined by the temporal coherence property of the light source while the lateral PSF is determined by the imaging optics in the sample arm. Furthermore, in Gaussian optics model, $h_{x,y}(x,y)$ is the product of PSFs in x and y dimensions $h_x(x)$ and $h_y(y)$ [21]. Therefore, we have

NIH-PA Author Manuscript

NIH-PA Author Manuscript

NIH-PA Author Manuscript

$$r_a(z)=h_{x,y}(x,y)*r_s(x,y,z)\big|_{y=0} \quad (1)$$

Here, * indicates convolution; $h_x(x)$ and $h_y(y)$ can be expressed as $exp[-(4\ln 2)x^2/w_x^2]$ and $exp[-(4\ln 2)y^2/w_y^2]$, respectively. w_x and w_y are the FWHM of the Gaussian shaped lateral impulse response of the imaging system in x and y directions. w_x and w_y are identical if the beam is circular. In addition, w_x and w_y are assumed to be constant for the entire imaging range, which is appropriate for a weakly focused beam.

Therefore, $S(x,k)$ can be expressed as:

$$S(x,k)=\alpha r_r S_0(k)\mathrm{Re}\left[\int_{-\infty}^{-\infty} r_a(z)\,e^{-j2kz}dz\right] \quad (2)$$

Here, α is a system responsive factor; r_r is the reference field reflectivity; $S_0(k)$ indicates the Gaussian shaped source spectrum and $S_0(k)=s_0\exp(-4\ln 2(k-k_0)^2/\Delta k^2)$ with s_0 as a constant indicating the magnitude of the source spectrum, k_0 as the center of the source spectrum and Δk as the spectral full width half maximum (FWHM). Re( ) stands for taking the real part of a complex value; j is the unit imaginary number. Eq. (2) assumes optical path lengths in reference and sample arms are identical for z=0. In the following analysis, we neglect the Re( ) operator, but it is worth mentioning that performing FFT on real valued spectral signals leads to complex conjugate ambiguity in OCT images [27].

Denote $h_y(0)*r_s(x,0,z)$ as $N_s(x,z)$, which can be expressed explicitly:

$$N_s(x,z)=\int_{-\infty}^{+\infty} h_y(-y')\,r_s(x,y',z)\,dy' \quad (3)$$

Spatial domain OCT signal $S(x,z)$ is obtained by taking the inverse Fourier Transform of Eq (2):

$$S(x,z)=\int_{k_0-\frac{\delta k}{2}}^{k_0+\frac{\delta k}{2}} \alpha r_r S_0(k)\left[\int_{-\infty}^{-\infty} h_x(x)*N_s(x,z')e^{-j2kz'}dz'\right]e^{j2kz}dk \quad (4)$$

In Eq. (4), δk indicates the spectral range of the spectrometer (for spectral domain FD OCT) or the sweeping range of the tunable laser source (for swept source FD OCT). With the FWHM bandwidth of the light source Δk sufficiently smaller than δk, integral over k in the range $[k-\delta k/2,\ k+\delta k/2]$ can be approximated by integral over k in the range $(-\infty, +\infty)$. Replacing the variable k with $k'=k-k_0$ in Eq. (4), changing the order of integration so that integral over wavenumber is performed first, and expanding the integration range from $-\infty$ to $+\infty$, we have:

$$\begin{aligned} S(x,z)&=\int_{-\frac{\delta k}{2}}^{\frac{\delta k}{2}} \alpha r_r s_0 e^{-4\ln 2\frac{k^2}{\Delta k^2}}\left\{\int_{-\infty}^{-\infty}\left[h_x(x)*N_s(x,z')\right]e^{-j2kz'}dz'\right\}e^{j2kz}dk \\ &\approx \alpha r_r s_0\int_{-\infty}^{-\infty}\left[h_x(x)*N_s(x,z')\right]e^{j2k_0(z-z')}\left[\int_{-\infty}^{+\infty} e^{j2k(z-z')}e^{-4\ln 2\frac{k^2}{\Delta k^2}}dk\right]dz' \end{aligned} \quad (5)$$

The integration over variable k is in fact the Fourier transform of Gaussian:

NIH-PA Author Manuscript

NIH-PA Author Manuscript

NIH-PA Author Manuscript

$$\int_{-\infty}^{+\infty} e^{j2k(z-z')} e^{-4\ln 2\frac{k^2}{\Delta k^2}} dk = \Delta k \sqrt{\frac{2\pi}{8\ln 2}} e^{-4\ln 2\frac{(z-z')^2}{w_z^2}} \quad (6)$$

Therefore, we have:

$$S(x,z) \approx \beta \int_{-\infty}^{-\infty} \left[h_x(x) * N_s(x,z') \right] e^{j2k_0(z-z')} e^{-4\ln 2(z-z')^2/w_z^2} dz' \quad (7)$$

In the Eq (7), $\beta = \Delta k \alpha r_r s_0/(8\ln 2)^{1/2}$ and $w_z = 4\ln 2/\Delta k$. Denote $exp(j2k_0 z)exp(-4\ln 2 z^2/w_z^2)$ as $h_z(z)$, we have:

$$\begin{aligned} S(x,z) &\approx \beta \int_{-\infty}^{-\infty} \left[h_x(x) * N_s(x,z') \right] h_z(z-z') dz' \\ &= \beta \left[h_x(x) h_z(z) \right] * N_s(x,z) \end{aligned} \quad (8)$$

Describing the sample field reflectivity $N_s(x,z)$ as a collection of scatterers that are randomly distributed, we can model the object $N_s(x,z)$ as summation of 2D Dirac functions:

$$N_s(x,z) = \sum_n a_n \delta(x - x_n, z - z_n) \quad (9)$$

In Eq. (9), (x_n, z_n) indicates the location of the nth scatterers; a_n indicates the amplitude of signal from the nth scatterer.

In practice, pixels in OCT images have finite pixel widths Δx and Δz in lateral and axial dimensions. Considering the pixel dimension, $S_P(x,z)$, OCT signal at pixel (x, z) is:

$$\begin{aligned} S_p(x,z) &= S(x,z) * rect\left(\frac{x}{\Delta x}, \frac{z}{\Delta z}\right) \\ &= \beta \left[h_x(x) h_z(z) \right] * \left[N_s(x,z) * rect\left(\frac{x}{\Delta x}, \frac{z}{\Delta z}\right) \right] \\ &= \beta h_{x,z}(x,z) * N_p(x,z) \end{aligned} \quad (10)$$

In Eq (10), $h_{x,z}(x,z)$ indicates $h_x(x)h_z(z)$.

$N_P(x, z)$ can be calculated:

$$N_p(x,z) = \sum_n a_n \left[\int_{x-\frac{\Delta x}{2}}^{x+\frac{\Delta x}{2}} \int_{z-\frac{\Delta z}{2}}^{z+\frac{\Delta z}{2}} \delta(x' - x_n, z' - z_n) dx' dz' \right] = \sum_{n=1}^{m} a_n \quad (11)$$

Here, m is the number of scatterers within the pixel located at (x,z). Eq (11) implies that Np follows a Poisson distribution. Moreover if m is large enough (>5), $N_P(x,z)$ can be described as a Gaussian random variable according to central limit theorem [24]. In our program, we generated 2D normally distributed random field to model $N_P(x,z)$. In practice, the statistical distribution of N_p can be determined by the voxel dimension and the size of scatterer of interest.

NIH-PA Author Manuscript

NIH-PA Author Manuscript

NIH-PA Author Manuscript

To synthesize a speckle pattern based on this model, one generates 2D PSF in x-z plane to represent the property of the imaging system and 2D random object; and then convolves the PSF with the random object field. Arbitrary PSF can be used. With different spatial locations, random variables ($N_P(x,z)$) with different statistical properties can be generated to represent scatterers with heterogeneous spatial distribution. Due to the procedure of signal generation of our method, this simulation is referred as spatial domain simulation (SD simulation) in this manuscript. To validate our model, we also implemented a speckle simulation method proposed by D. Duncan *et al* with slight modifications and referred this method as frequency domain simulation (FD simulation), because their method generates speckle patterns by Fourier transforming band-limited frequency domain random field [25].

3. Simulated speckle pattern and its statistical properties

Assuming an OCT system operates with a central wavelength of 840nm, and has a Gaussian shaped PSF with 6μm FWHM in axial direction and a Gaussian shaped PSF with 10μm FWHM lateral direction, we simulated OCT PSF as shown in Figure 1 (a), (b) and (c). Figure 1 (a) shows the magnitude (blue), real part (red) and imaginary part (black) of the complex valued axial PSF $h_z(z)$; Figure 1 (b) shows the lateral PSF $h_x(x)$; Figure 1(c) shows the 2D PSF $h_{x,z}(x,z)$ (magnitude). We generate a matrix with random variables as a 2D normally distributed random field $N_P(x,z)$. The mean and standard deviation of these random variables are both 1. To obtain the OCT speckle pattern shown in Figure 1 (d), we convolved the $h_{x,z}(x,z)$ in Figure 1(c) with $N_P(x,z)$, took the magnitude of the convoluted image and rescale the magnitude of the image so that pixel values ranged from 0 to 1.

To validate our simulation method, we compared results of our simulation with the one obtained from a method proposed by D. Duncan *et al* [25]. In their simulation, the authors filled a circular region of diameter D of a $L\times L$ matrix with complex random numbers. The amplitudes of these random numbers were unity and the phases were uniformly distributed over ($-\pi$, $+\pi$). To synthesize a spatially band limited speckle pattern, a 2D Fourier transform was performed on the $L\times L$ array. In fact, the spatial bandwidth of an image is determined the bandwidth of modulation transfer function (MTF) of the imaging system or the width of PSF. Essentially, an ideal low pass filter was applied to the broadband signal to generate band limited speckle patterns in D. Duncan *et al*'s simulations. However, the spatial frequency component of a real image does not have an infinitely sharp cut-off frequency as simulated in [25]. Therefore, we implemented D. Duncan *et al*'s with a slight modification. In our simulation, we filled a matrix with complex numbers of unity amplitude and with phases uniformly distributed over ($-\pi$, $+\pi$), filtered it with 2D MTF which is the Fourier transform of the 2D PSF $h_{x,z}(x,z)$and performed 2D Fourier transform to obtain OCT speckle pattern. The axial MTF, lateral MTF, 2D MTF and synthesized OCT image are shown in Figure 1 (e), (f), (g) and (h).

The PDF and PSD of OCT speckle pattern were calculated from images generated with SD and FD simulation. Figure 2 (a) shows the PDF (P_i, i=1,2,…,N, N is the number of bins used to calculate PDF) obtained from the SD simulated OCT speckle patterns as red dots. Assuming the PDF follows a Rayleigh distribution $P_R(S)$, as expressed by Eq (12), we can obtain a maximum likelihood estimator of the parameter σ by calculating $[\Sigma(P_i^2)/(2N)]^{1/2}$. The Rayleigh distribution corresponding to the obtained σ is shown as black curve in Figure 2(a). The difference between the estimated Rayleigh distribution and the simulated PDF is shown as the blue curve.

$$P_R(S)=\frac{S}{\sigma^2}e^{-S^2/2\sigma^2} \quad (12)$$

NIH-PA Author Manuscript

NIH-PA Author Manuscript

NIH-PA Author Manuscript

In addition, we also calculated the PSD of the speckle pattern generated by SD simulation and show the normalized and then logarithm scaled PSD in Figure 2(b). For comparison, we did the same analysis to OCT speckle pattern generated by the FD simulation and show the results in Figure 2(c) and (d).

In Figure 2 (a) and (c), the consistency between simulated result (black curve) and Rayleigh distribution (red curve) suggests that we have generated a speckle pattern with Rayleigh distribution using either SD or FD simulation which is consistent with previous studies [4, 23]. Moreover, the estimated value of σ for Rayleigh distribution are 0.2381 and 0.2402 for SD and FD simulations shown in Figure 2, respectively. These values are close enough so that we can consider that the PDFs generated from SD and FD simulations are identical. It is worth mentioning that as the amplitude of OCT signal demonstrates Rayleigh distribution, the intensity of OCT signal (square of amplitude) flows a negative exponential distribution, according to the property of random variable transformation.

PSDs in Figure 2 (b) and (c) show the same oblong shape. The major axis of the ellipses is along axial direction, because the axial resolution in our simulation was higher than the lateral resolution.

In conclusion, the SD speckle simulation proposed in this paper generates Rayleigh distributed OCT signal as the FD simulation which has been used for speckle analysis in several studies. The FD method can only simulate global features of the speckle pattern; while our SD method can simulate speckle pattern with spatial heterogeneity. For example, we can generate $N_P(x,z)$ with different mean and variance at different spatial location to represent a heterogeneous sample.

4. Statistics of XCC obtained from OCT speckle pattern

4.1. General statistics of XCC

Speckle decorrelation has been used for motion tracking in ultrasound imaging, as well as in OCT [19–21, 28, 29]. In our previous work, we calculated Pearson cross correlation coefficient (XCC) between adjacent A-scans to quantify the degree of speckle decorrelation due to lateral motion. XCC calculated from A-scans that are displaced by Δx is denoted as $\rho_{\Delta x}$, which can be calculated according to Eq (13):

$$\rho_{\Delta x}=\frac{\langle[I_x(z)-\langle I_x(z)\rangle][I_{x+\Delta x}(z)-\langle I_{x+\Delta x}(z)\rangle]\rangle}{\sigma_{I_x(z)}\sigma_{I_{x+\Delta x}(z)}} \quad (13)$$

In Eq (13), < > indicates to take the mean of a random signal; $I_x(z)$ is the intensity of an A-scan at lateral coordinate x: $I_x(z) = S(x,z)S^*(x,z)$. $I_{x+\Delta x}(z)$ is the intensity of A-scan that is displaced by Δx. $\sigma_{Ix(z)}$ and $\sigma_{Ix+\Delta x(z)}$ are the square roots of variance for $I_x(z)$ and $I_{x+\Delta x}(z)$. It is worth mentioning that $\rho_{\Delta x}$ is also a random variable. In other words, the value of $\rho_{\Delta x}$ obtained from an arbitrary experiment with a given Δx may be different in different measurement and is generally different from its expectation value which can be calculated with Eq (14) [21]:

$$E(\rho_{\Delta x})=\exp\left[-\frac{(\Delta x)^2}{w_x^2}\right] \quad (14)$$

On the other hand, displacement can be estimated by Eq (15), assuming the value of XCC obtained experimentally is a good approximation of its expectation value.

NIH-PA Author Manuscript

NIH-PA Author Manuscript

NIH-PA Author Manuscript

$$\Delta x = w_x \sqrt{\ln\left(\frac{1}{\rho_{\Delta x}}\right)} \quad (15)$$

Eq (15) was theoretically derived and experimentally validated in our previous work [21]. To evaluate the accuracy and to optimize the performance of the speckle decorrelation algorithm, it is desirable to obtain a more comprehensive statistical appreciation of XCC. Using our SD simulation to synthesize a 2D OCT speckle pattern, we calculated values of XCC with different lateral displacement Δx. 500 independent, random speckle patterns were generated and therefore 500 sets of values of $\rho_{\Delta x}$ for each displacement were obtained. $P_\rho(\Delta x,r)$, the probability for XCC obtained with displacement Δx to take a value of r was calculated using values obtained from simulation and the results are shown in Figure 3 (a). In Figure 3 (a), each vertical line corresponds to a value of displacement and each horizontal line corresponds to a value of ρ; the probability value $P_\rho(\Delta x,r)$ is encoded as the color of the image: dark red indicates 1 and dark blue indicates 0 as shown in the colorbar of Figure 3 (a). To display $P_\rho(\Delta x,r)$, a 2D matrix with large dynamic range, we took the logarithm of $P_\rho(\Delta x,r)$ and displayed the result using jet colormap in Matlab. Figure 3 (a) shows that ρ decreases as lateral displacement Δx. Moreover, the distribution of $P_\rho(\Delta x,r)$ gets broadened with increased Δx. In other words, if one uses the decorrelation of speckle to estimate motion, the result is less accurate if ρ is calculated using A-scans far away from each other. In Figure 3 (b), we show the averaged value of $\rho_{\Delta x}$ as black circles. For comparison, we also plot the relationship shown in Eq (14) as the red curve in Figure 3(b). Consistency between results from simulation and theoretical calculation can be observed in Figure 3 (b). In Figure 3 (c), we show σ_ρ^2, the variance of the each cross correlation coefficient. With small Δx, σ_ρ^2 increases as displacement between A-scans used for calculation; afterwards, σ_ρ^2 reaches a plateau, when displacement is large so that A-scans are completely decorrelated and cross correlation coefficient represents merely statistical noise. For accurate displacement estimate, the A-scans involved in the calculation has to be displaced of a small enough value so that σ_ρ^2 has to be smaller than the value at the plateau. According to Figure 3 (c), this requires the displacement between A-scans used for correlation calculation to be smaller than approximately 5μm. This conclusion is also consistent with the Nyquist sampling theorem, which requires to sample twice as fast as the highest spatial frequency. In our simulation, the lateral resolution is 10μm; therefore the sampling interval must be smaller than half of this value which is 5μm.

4.2 XCC from signal with exponential decay

Due to signal loss from scattering and absorption, OCT signal often decays with imaging depth exponentially and this might result in a speckle decorrelation curve different from the results shown in Figure 3 (b). To simulate this scenario using our SD simulation, we generated a spatially homogeneous 2D random matrix; multiplied each depth profile generated with an exponential decay function $a(z) = exp(-z/z_0)$. Here, we chose the value of z_0 to be 50μm. Afterwards, we convolved the 2D object generated with the system PSF, same as the one shown Figure 2 (c). One of the simulated A-scan with exponential decay is shown in Figure 4(a), green curve. Using the generated OCT image with exponential decay, we obtained XCC, $\rho_{\Delta x,decay}$, as green circles in Figure 4(b). $\rho_{\Delta x,decay}$ has larger values compared to the theoretical values shown as the red curve. As a result, using $\rho_{\Delta x,decay}$ to calculate displacement through Eq (15) would result in a smaller displacement estimation than the actual displacement.

To correct for this effect, we averaged multiple A-scans. The averaging essentially served as a low pass filter and removed drastic signal fluctuation between A-scans due to speckle. We thereafter performed exponential fitting on the profile obtained from averaging to obtain

NIH-PA Author Manuscript

NIH-PA Author Manuscript

NIH-PA Author Manuscript

$\tilde{a}(z)$, an exponential decay function that approximated $a(z)$. To correct the decay, we divided the simulated OCT signal shown as the green curve in Figure 4 (a) with $\tilde{a}(z)$. After such correction, the green curve in Figure 4 (a) became the black curve. We calculated XCC based on the exponential decay correction and show the results as black circles in Figure 4 (b). The consistency between the red curve and black circles indicates that one can extract displacement with higher accuracy using XCC obtained from exponential decay corrected OCT signal.

In reality, the implementation of this correction might be difficult because signal does not decay exponentially in the presence of tissue boundaries in the axial direction. Even if the signal decays exponentially, the decay constant might be different at different lateral locations. If the average is performed on a limited number of A-scans with the same exponential decay, the smoothing effect might not be significant and therefore simple curve fitting cannot deduce the actual exponential decay function accurately. It is also worth mentioning, the obtained exponential decay function might have extremely small values at large of z. The correction procedure that involves dividing OCT signal extremely small values (~0) might significantly increase the overall noise level.

4.3 XCC from speckle pattern with lateral heterogeneity

To study the effect of lateral heterogeneity on the XCC calculation and displacement estimation, we generated a matrix consisting of random sub-matrices with different variances; and then convolved the generated matrix with 2D PSF shown as Figure 1 (c). The resultant speckle pattern is shown as Figure 5 (a). The bright and dark stripes correspond to different Gaussian random matrices M_1 and M_2. The variance of M_1 is 4 times larger than that of M_2; while M_1 and M_2 have the same mean. We subsequently calculated the XCC from the generated speckle pattern using adjacent A-scans at different lateral locations. The obtained result is shown as red curve in Figure 5(b). We also generated a homogeneous speckle pattern using Gaussian random matrix with the same mean and variance as M_1 and calculated XCC in a same manner. The XCC corresponding to the homogeneous speckle pattern is shown as green curve in Figure 5(b). We also averaged signal along axial direction and show the averaged signal amplitude as black curve in Figure 5(b). It is seen that XCC drops slightly with a signal discontinuity. In another simulation, we used Gaussian random matrices M_1 and M_2 with 16 times difference in variance to the simulated speckle pattern. The obtained results are shown in Figure 5 (c) and (d). A larger drop in XCC can be observed in Figure 5 (d) due to a larger contrast between different parts of the sample.

When signal decorrelation due to structural difference is interpreted as signal decorrelation due to lateral displacement, the estimated lateral displacement is larger than its actual value. However, the drop of XCC only happens at pixels corresponding to structural boundary. Therefore, only a small amount of A-scans will cause inaccurate displacement estimation. Therefore, the overall performance of the speckle decorrelation algorithm can be considered as unaffected by such effect.

4.4 XCC from speckle pattern with axial heterogeneity

We generated an OCT speckle pattern with axial heterogeneity as shown in Figure 6 (a). The bright and dark stripes correspond to different Gaussian random matrices M_1 and M_2. The variance of M_1 is 4 times larger than that of M_2; while M_1 and M_2 have the same mean. XCC values were calculated from the generated speckle pattern using adjacent A-scans at different lateral locations and the results are shown as the red curve in Figure 6 (b). We also generated a homogeneous speckle pattern using a Gaussian random matrix with the same mean and variance as M_1 and calculated XCC in a same manner. The XCC corresponding to the homogeneous speckle pattern is shown as a green curve in Figure 6 (b). No significant

NIH-PA Author Manuscript

NIH-PA Author Manuscript

NIH-PA Author Manuscript

difference can be observed between the red and green curves in terms of mean XCC value. This is because A-scans with lateral displacements are involved in XCC calculation; therefore the result is independent of sample structure in axial dimension.

5.Discussion

We have recently shown that the speckle decorrelation properties of OCT signal is highly effective in obtaining sample motion speed, probe motion speed flow velocity, and scanning speed correction [20]. In these applications, a few A-scans were involved in the calculation of XCC for displacement extraction. Therefore the calculated XCC is local rather than global. As indicated by D. D. Duncan *et al* [26], the global speckle contrast calculated from an experimentally acquired, fully developed, speckle pattern shows good consistency with its theoretical value, the local speckle contrast obtained from a limited number of pixels is random and can be substantially different from its theoretical value. Therefore, a more accurate estimation of displacement can be deduced from XCC obtained from a larger set of A-scans within a given interval. In other words, oversampling is essential in motion estimation using speckle decorrelation methods. This is also consistent with results in Figure 3 (a): the XCC value obtained with small displacement has a narrower distribution.

Acknowledgments

The research reported in this paper was supported in part by NIH BRP grants 1R01 EB 007969, R21 1R21NS063131-01A1, NIH/NIE R011R01EY021540-01A1, and in part by fellowship support from the ARCS Foundation.

References

1. Goodman, JW. Statistical Optics. Wiley; New York: 1985.
2. Goodman JW. Some fundamental properties of speckle. J Opt Soc Am. 1976; 66:1145–1150.
3. Schmitt JM, Xiang SH, Yung KM. Speckle in optical coherence tomography. J Biomed Opt. 1999; 4(1):95. [PubMed: 23015175]
4. Pircher M, Götzinger E, Leitgeb R, Fercher AF, Hitzenberger CK. Speckle reduction in optical coherence tomography by frequency compounding. J Biomed Opt. 2003; 8:565. [PubMed: 12880365]
5. Adler DC, Ko TH, Fujimoto JG. Speckle reduction in optical coherence tomography images by use of a spatially adaptive wavelet filter. Opt Lett. 2004; 29:2878–2880. [PubMed: 15645810]
6. Marks DL, Ralston TS, Boppart SA. Speckle reduction by I-divergence regularization in optical coherence tomography. J Opt Soc Am A. 2005; 22:2366–2371.
7. Ozcan A, Bilenca A, Desjardins AE, Bouma BE, Tearney GJ. Speckle reduction in optical coherence tomography images using digital filtering. J Opt Soc Am A. 2007; 24:1901–1910.
8. Desjardins AE, Vakoc BJ, Oh WY, Motaghiannezam SM, Tearney GJ, Bouma BE. Angle-resolved Optical Coherence Tomography with sequential angular selectivity for speckle reduction. Opt Express. 2007; 15:6200–6209. [PubMed: 19546925]
9. Kennedy BF, Hillman TR, Curatolo A, Sampson DD. Speckle reduction in optical coherence tomography by strain compounding. Opt Lett. 2010; 35:2445–2447. [PubMed: 20634858]
10. Jian Z, Yu L, Rao B, Tromberg BJ, Chen Z. Three-dimensional speckle suppression in optical coherence tomography based on the curvelet transform. Opt Express. 2010; 18:1024–1032. [PubMed: 20173923]
11. Gossage KW, Tkaczyk TS, Rodriguez JJ, Barton JK. Texture analysis of optical coherence tomography images: feasibility for tissue classification. J Biomed Opt. 2003; 8:570. [PubMed: 12880366]
12. Kasaragod DK, Lu Z, Smith LE, Matcher SJ. Speckle texture analysis of optical coherence tomography images. Proc SPIE. 2010; 7387:73871V.

NIH-PA Author Manuscript

NIH-PA Author Manuscript

NIH-PA Author Manuscript

13. Gossage KW, Smith CM, Kanter EM, Hariri LP, Stone AL, Rodriguez JJ, Williams SK, Barton JK. Texture analysis of speckle in optical coherence tomography images of tissue phantoms. Phys Med Biol. 2006; 51:1563–1575. [PubMed: 16510963]
14. Barton J, Stromski S. Flow measurement without phase information in optical coherence tomography images. Opt Express. 2005; 13:5234–5239. [PubMed: 19498514]
15. Mariampillai A, Standish BA, Moriyama EH, Khurana M, Munce NR, Leung MKK, Jiang J, Cable A, Wilson BC, Vitkin IA, Yang VXD. Speckle variance detection of microvasculature using swept-source optical coherence tomography. Opt Lett. 2008; 33(13):1530–1532. [PubMed: 18594688]
16. Mariampillai A, Leung MKK, Jarvi M, Standish BA, Lee K, Wilson BC, Vitkin A, Yang VXD. Optimized speckle variance OCT imaging of microvasculature. Opt Lett. 2010; 35(8):1257–1259. [PubMed: 20410985]
17. Liu X, Zhang K, Huang Y, Kang JU. Spectroscopic-speckle variance OCT for microvasculature detection and analysis. Biomed Opt Express. 2011; 2:2995–3009. [PubMed: 22076262]
18. Cadotte DW, Mariampillai A, Cadotte A, Lee KKC, Kiehl T, Wilson BC, Fehlings MG, Yang VXD. Speckle variance optical coherence tomography of the rodent spinal cord: in vivo feasibility. Biomed Opt Express. 2012; 3:911–919. [PubMed: 22567584]
19. Motaghiannezam R, Fraser S. Logarithmic intensity and speckle-based motion contrast methods for human retinal vasculature visualization using swept source optical coherence tomography. Biomedical Opt Express. 2012; 3:503–521.
20. Ahmad A, Adie SG, Chaney EJ, Sharma U, Boppart SA. Cross-correlation-based image acquisition technique for manually-scanned optical coherence tomography. Opt Express. 2009; 17:8125–8136. [PubMed: 19434144]
21. Liu X, Huang Y, Kang JU. Distortion-free freehand-scanning OCT implemented with real-time scanning speed variance correction. Opt Express. 2012; 20:16567–16583.
22. Bashkansky M, Reintjes J. Statistics and reduction of speckle in optical coherence tomography. Opt Lett. 2000; 25:545–547. [PubMed: 18064106]
23. Karamata B, Hassler K, Laubscher M, Lasser T. Speckle statistics in optical coherence tomography. J Opt Soc Am A. 2005; 22:593–596.
24. Meunier J, Bertrand M. Ultrasonic texture motion analysis: Theory and simulation. IEEE Trans Med Imag. 1995; 14(2):293–300.
25. Kirkpatrick SJ, Duncan DD, Wang RK, Hinds MT. Quantitative temporal speckle contrast imaging for tissue mechanics. J Opt Soc Am A. 2007; 24:3728–3734.
26. Duncan DD, Kirkpatrick SJ, Wang RK. Statistics of local speckle contrast. J Opt Soc Am A. 2008; 25:9–15.
27. Choma M, Sarunic M, Yang C, Izatt J. Sensitivity advantage of swept source and Fourier domain optical coherence tomography. Opt Express. 2003; 11:2183–2189. [PubMed: 19466106]
28. Chen JF, Fowlkes JB, Carson PL, Rubin JM. Determination of scan-plane motion using speckle decorrelation: theoretical considerations and initial test. Int J Imaging Syst Technol. 1997; 8(1): 38–44.
29. Li PC, Cheng CJ, Yeh CK. On velocity estimation using speckle decorrelation. IEEE Trans Ultrason Ferroelectr Freq Control. 2001; 48(4):1084–1091. [PubMed: 11477767]

NIH-PA Author Manuscript

NIH-PA Author Manuscript

NIH-PA Author Manuscript

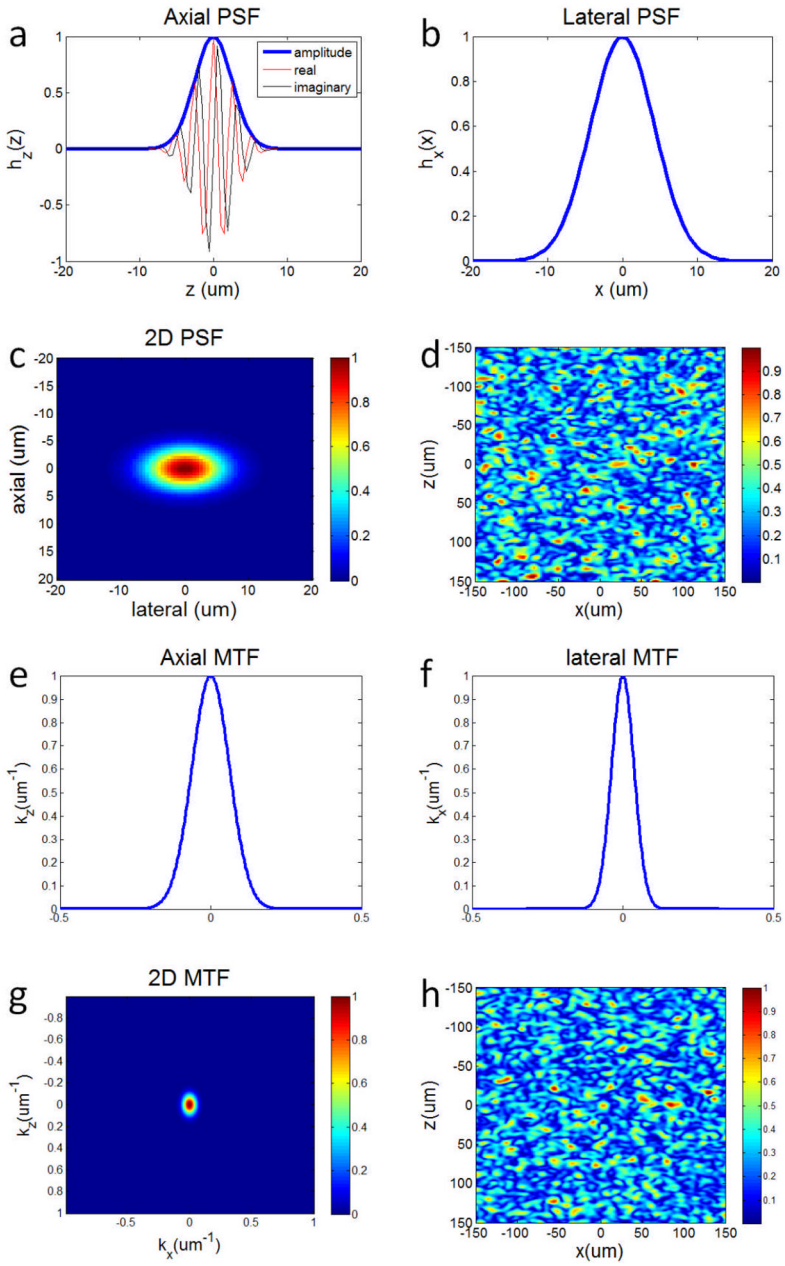

Figure 1.

(a) $h_z(z)$, the axial PSF of OCT system (blue: magnitude; red: real part; black: imaginary part); (b) $h_x(x)$, the lateral PSF of OCT system; (c) $h_{x,z}(x,z)$, 2D PSF; (d) synthesized OCT speckle pattern from spatial domain simulation; (e) axial MTF; (f) lateral MTF; (g) 2D MTF; (h) synthesized OCT speckle pattern from frequency domain simulation.

NIH-PA Author Manuscript

NIH-PA Author Manuscript

NIH-PA Author Manuscript

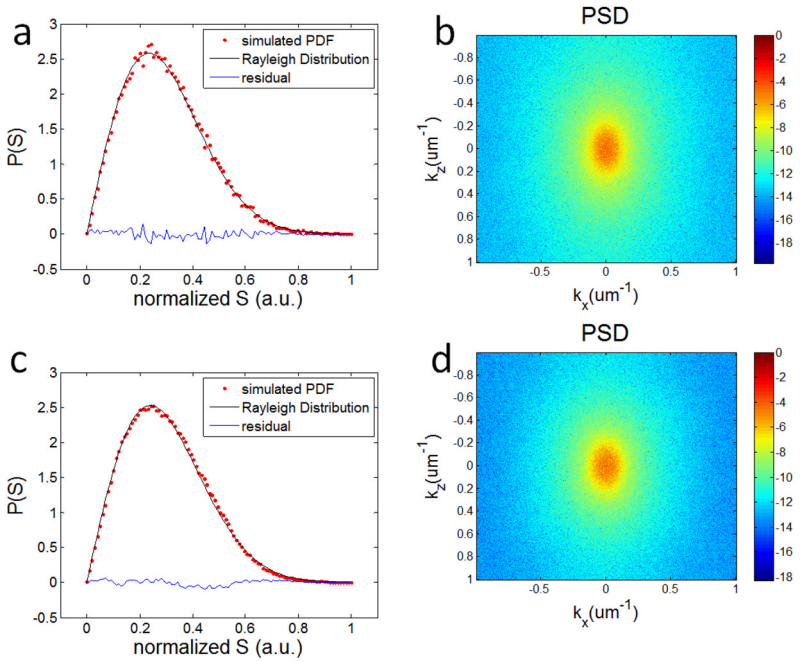

Figure 2.

(a) PDF of OCT speckle pattern obtained from SD simulation; (b) PSD of OCT speckle pattern obtained from SD simulation; (c) PDF of OCT speckle pattern obtained from FD simulation; (d) PSD of OCT speckle pattern obtained from SD simulation.

NIH-PA Author Manuscript

NIH-PA Author Manuscript

NIH-PA Author Manuscript

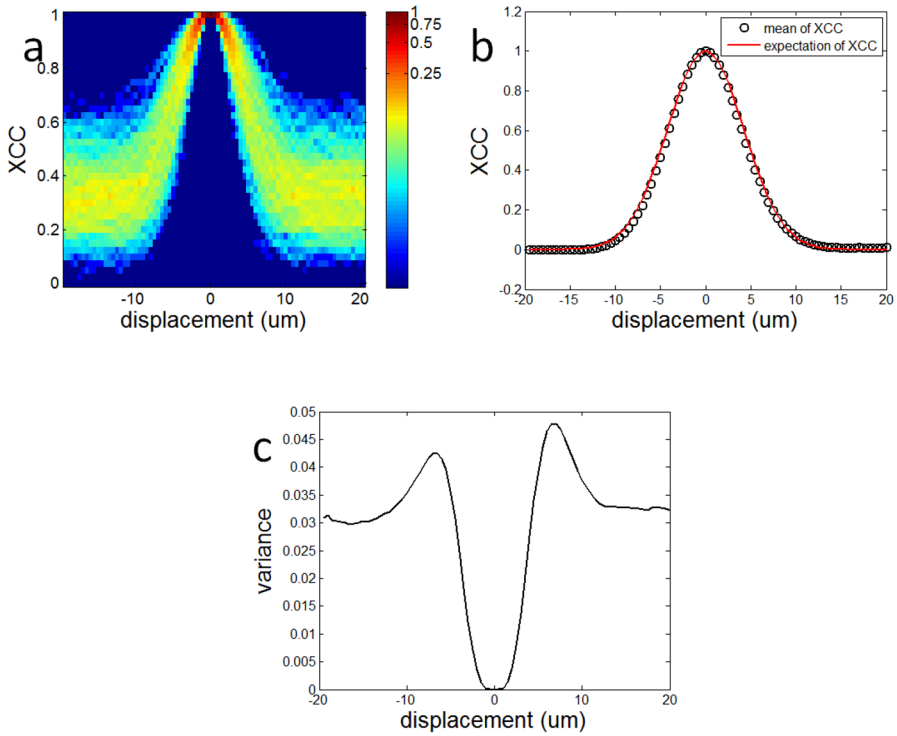

Figure 3.

(a) The probability for $\rho_{\Delta x}$ to take different values; (b) mean value of $\rho_{\Delta x}$ from simulation (black circles) as compared with the expectation of $\rho_{\Delta x}$ from theoretical calculation (red curve); (c) variance of $\rho_{\Delta x}$ at different displacement

NIH-PA Author Manuscript

NIH-PA Author Manuscript

NIH-PA Author Manuscript

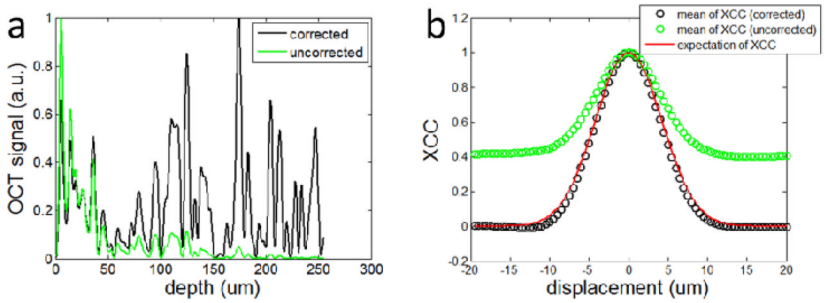

Figure 4.

(a) OCT signal with exponential decay (green) and after exponential decay correction (black); (b) XCC calculated using OCT signal with exponential decay (green circles); XCC calculated using OCT signal after exponential decay correction (black circles); and theoretical XCC values (red)

NIH-PA Author Manuscript

NIH-PA Author Manuscript

NIH-PA Author Manuscript

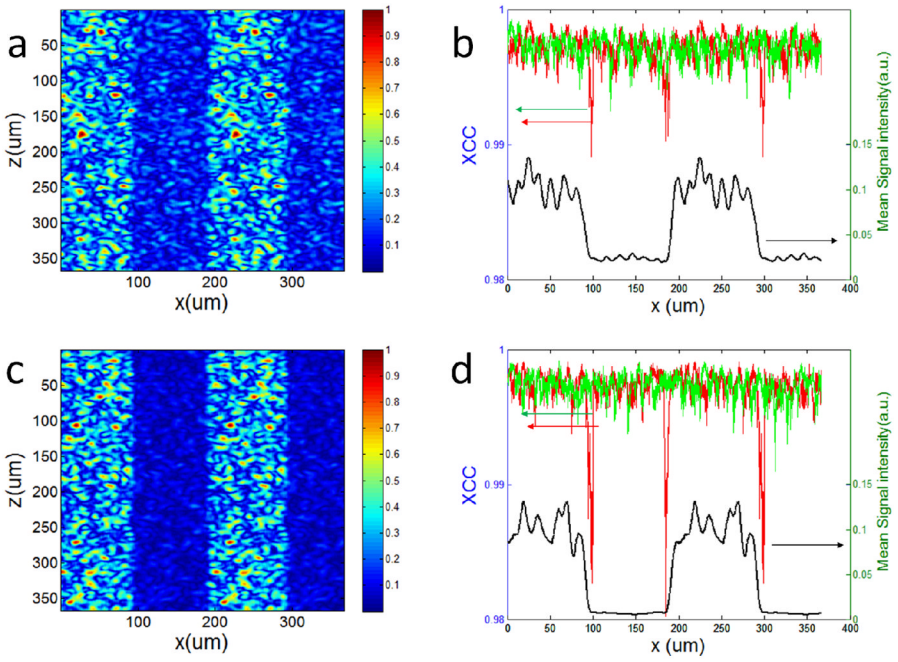

Figure 5.

(a) speckle pattern with lateral heterogeneity generated from Gaussian random matrices M_1 and M_2; the variance of M_1 is 4 times larger than that of M_2; (b) XCC calculated from the speckle pattern shown in Figure 5 (a) using adjacent A-scans at different lateral locations; (c) speckle pattern with lateral heterogeneity generated using Gaussian random matrices M_1 and M_2; the variance of M_1 is 16 times larger than that of M_2; (d) XCC calculated from the speckle pattern shown in Figure 5 (c) using adjacent A-scans at different lateral locations.

NIH-PA Author Manuscript

NIH-PA Author Manuscript

NIH-PA Author Manuscript

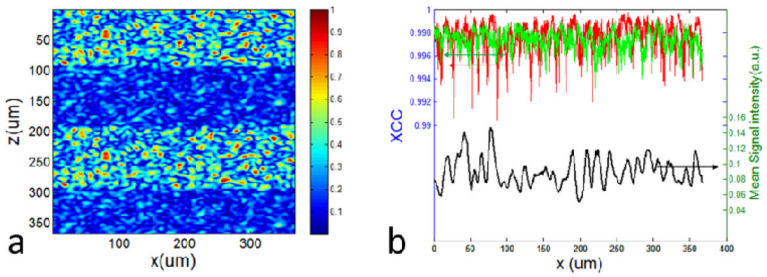

Figure 6.

(a) speckle pattern with axial heterogeneity generated using Gaussian random matrices M_1 and M_2; the variance of M_1 is 4 time larger than that of M_2; (b) XCC calculated from the speckle pattern shown in Figure 6 (a) using adjacent A-scans in different lateral locations.